Journal of ELECTRONIC MATERIALS, Vol. 46, No. 5, 2017
DOI: 10.1007/s11664-016-5035-y

Phase Formation and Thermoelectric Properties of Doped Higher Manganese Silicides ($Mn_{15}Si_{26}$)

HWIJONG LEE,[1] GWANSIK KIM,[1] BYUNGHUN LEE,[1] KYU HYOUNG LEE,[2,3] and WOOYOUNG LEE[1,4]

1.—Department of Materials Science and Engineering, Yonsei University, Seoul 03722, South Korea. 2.—Department of Nano Applied Engineering, Kangwon National University, Chuncheon 24341, South Korea. 3.—e-mail: khlee2014@kangwon.ac.kr. 4.—e-mail: wooyoung@yonsei.ac.kr

We herein report substitutional doping effects on the electronic and thermal transport properties of higher manganese silicides (HMS) $Mn_{15}Si_{26}$. Polycrystalline bulks of $Mn_{0.972}A_{0.028}Si_{1.80}$ and $MnSi_{1.75}B_{0.028}$ (A = V, Cr, Mo/B = Al, Ge) were fabricated by a solid-state reaction combined with the spark plasma sintering technique, and their thermoelectric properties were evaluated. We found that thermoelectric performance of $Mn_{15}Si_{26}$ was significantly enhanced due to the simultaneous improvement in electronic transport and phonon scattering via partial substitution of foreign atoms at Mn- and/or Si-sites. Through the small amount of Cr doping at the Mn-site and Al and Ge doping at the Si-site, the power factor was improved due to enhancement in density of the state's effective mass. Thermal transport properties could be also manipulated due to the point defect phonon scattering effect, and reduced lattice thermal conductivity was obtained with Ge-doped HMS. As a consequence, the maximum dimensionless figure of merit ZT of 0.64 at 773 K (increased 50% compared to undoped $Mn_{15}Si_{26}$) was obtained in Ge-doped $Mn_{15}Si_{26}$.

Key words: Substitutional doping, higher manganese silicide, thermoelectric, phonon scattering, density of states effective mass

INTRODUCTION

Silicide-based materials made of earth-abundant and non-toxic elements became known as one of the most promising candidates for materials of thermoelectric power generation (TEG) at intermediate temperature (500–800 K). For the extensive application of TEG systems, it is crucial to realize excellent thermoelectric (TE) performance in both n- and p-type materials. The performance of a TE material is demonstrated using the dimensionless figure of merit $ZT = \sigma S^2 T/\kappa$, where σ, S, κ, and T represent electrical conductivity, Seebeck coefficient, thermal conductivity and the absolute temperature, respectively. High ZT materials promote the high performance of applications of TEG systems. Among transition metal silicides, higher manganese silicides (HMS) are considered as promising p-type TE materials, which pair up with n-type Mg_2Si-based materials due to their relatively high ZT value and good chemical stability.[1] The complex crystal structure of HMS, an obvious example of Nowotny chimney ladder (NCL) phases,[2] consists of four distinct phases including Mn_4Si_7, $Mn_{11}Si_{19}$, $Mn_{15}Si_{26}$, and $Mn_{27}Si_{47}$. Intrinsic low κ of HMS originated from these complex crystal structures due to a large phase space for acoustic phonon scattering by their low-lying optical vibration modes, and resulted in relatively high ZT value among p-type silicides.[3] However, the maximum ZT value of HMS has been limited to 0.6 owing to its relatively low electron transport properties (σ and S), thus the exploration of new approaches for enhancement of ZT in HMS systems is an urgent

(Received June 7, 2016; accepted October 6, 2016; published online October 21, 2016)

requirement for the realization of total silicide TE modules for mid-temperature TEG applications.

Continuous efforts to enhance the *ZT* value of HMS has been conducted to achieve two main purposes: (1) improvement of the power factor (σS^2) and (2) suppression of κ by reduction of lattice thermal conductivity ($\kappa_{lat} = \kappa - \kappa_{ele}$). One widely used approach is nanostructuring[13–16] for reduced κ_{lat} such as nanograin and nanoinclusion composites, however, *ZT* enhancement is limited in HMS owing to the intrinsically low κ. Thus well controlled defect structures for intensified phonon scattering should be introduced for an efficient κ_{lat} reduction. Another approach is compositional tuning by substitutional doping,[4–12] which has been reported to be an effective way to both increase the power factor and reduce thermal conductivity. For example, a peak *ZT* of 0.64 at 823 K was obtained in Re-doped HMS.[8,9] Combined techniques of nanostructuring and compositional tuning would be a promising approach for an enhanced *ZT* for HMS.

In the present study, we prepared the V-, Cr- or Mo-doped (Mn-site) and Al- or Ge-doped (Si-site) $Mn_{15}Si_{26}$ in an effort to find base compositions for advanced processing approaches such as nanostructuring, expecting that group V or VI elements substituted at Mn-sites or group XIII or XIV elements substituted at Si-sites to modulate the electronic structure and phonon scattering behavior in the presence of substitutional point defects. Every doped $Mn_{15}Si_{26}$ polycrystalline bulk fabricated by a solid state reaction (SSR) combined with the spark plasma sintering (SPS) technique in the same nominal composition. A quantitative analysis for the electronic and thermal transport parameters was performed to clarify the tunability of TE transport properties by substitutional doping. It was demonstrated that the highest *ZT* of 0.64 at 773 K was obtained in $MnSi_{1.75}Ge_{0.028}$ due to the synergetic effects of an enhanced power factor and reduced κ_{lat}.

EXPERIMENTAL PROCEDURES

Doped HMS polycrystalline bulks with compositions of $Mn_{0.972}A_{0.028}Si_{1.80}$ and $MnSi_{1.75}B_{0.028}$ (A = V, Cr, Mo/B = Al, Ge) were synthesized by a conventional SSR and SPS technique. Amounts of substituting elements selected at the constant value of 0.028, which was calculated from 1 at.% of the whole matrix, was done in order to figure out the effect of substituting elements in the same conditions. Undoped HMS polycrystalline bulks ($Mn_{15}Si_{26}$) were also prepared by identical procedures in order to investigate the effect of substitutions. The different atomic ratio of Mn/Si in the nominal compositions between pristine HMS ($Mn_{15}Si_{26}$) and doped HMS polycrystalline bulks is due to the generation of secondary phases of silicide, which required excess Si to fabricate the $Mn_{15}Si_{26}$ phase. Pure elemental Mn (99.95%), Si (99.9%), V (99.5%), Cr (99.99%), Mo (99.9%), Al (99.97%) and Ge (99.999%) powders were weighed in a proper ratio and mixed using a mortar. The mixtures were cold-pressed under 100 MPa to make pellets and placed into a tube-type furnace at 1273 K for 12 h under a dynamic vacuum to form solid solution compounds during the heat treatment. Acquired samples were pulverized into powders using ball milling and separated by sieving to obtain < 53 μm-diameter particles. Then, disk-shaped bulks (10 mm in diameter and 12 mm in thickness) were fabricated by SPS at 1273 K for 3 min in a vacuum under 60 MPa uniaxial pressure. Phase analysis for the SPSed samples was studied by the powder x-ray diffraction method (PXRD, Ultima IV/ME 200DX, Rigaku, Japan) with CuKα radiation. The microstructure of the samples was analyzed with a Field Emission Scanning Electron Microscope (FE-SEM, JEOL 7800F, USA) with an energy dispersive x-ray spectrometer (EDS). Bar-type samples (2 mm $\times$ 2 mm $\times$ 8 mm) were cut in perpendicular to the press direction, and σ and *S* values were measured at the temperature range from 300 K to 873 K in parallel by a standard four-probe method and a steady state method system (ZEM-3, ULVAC, Japan) in He atmosphere, respectively. Disk-type samples (10 mm in diameter and 1 mm in thickness) were cut in a plane parallel to the press direction, and thermal diffusivity (*D*) was measured in a vacuum using the laser flash method (Netszch LFA-457, Germany). The total thermal conductivity κ was calculated using the equation, $\kappa = DC_p\rho$, where C_p is the heat capacity measured by differential scanning calorimetry (DSC 8000, Perkin Elmer, USA), and ρ is the bulk density. The Hall effect measurement was performed in the van der Pauw configuration using a home-built apparatus under a constant magnetic field (1T). Due to the high carrier concentration of the HMS, the Hall carrier concentration (p_H) and Hall mobility (μ_H) were calculated using a single parabolic band (SPB) model without the consideration of the minority carriers.

RESULTS AND DISCUSSION

Figure 1 shows the x-ray diffraction patterns for doped $Mn_{15}Si_{26}$ prepared by SSR and SPS techniques. Dopants were chosen from group V (Vanadium) and group VI (Chromium, Molybdenum) for the Mn-site and group XIII (Aluminum) and group XIV (Germanium) for the Si-site. All patterns are indexed with $Mn_{15}Si_{26}$ as a major phase owing to different Si contents on the nominal compositions, while the minor secondary phases MnSi, Si and XSi_2 (X = V, Cr, Mo) were detected in some compositions, which formed during their phase formation processes. As shown in Fig. 1, relatively a large total quantity of secondary phases observed in $Mn_{0.972}V_{0.028}Si_{1.80}$ (7.77 wt.%) and $Mn_{0.972}Mo_{0.028}Si_{1.80}$ (8.40 wt.%) was compared to that of $MnSi_{1.75}Al_{0.028}$ (0.86 wt.%), $MnSi_{1.75}Ge_{0.028}$ (1.09

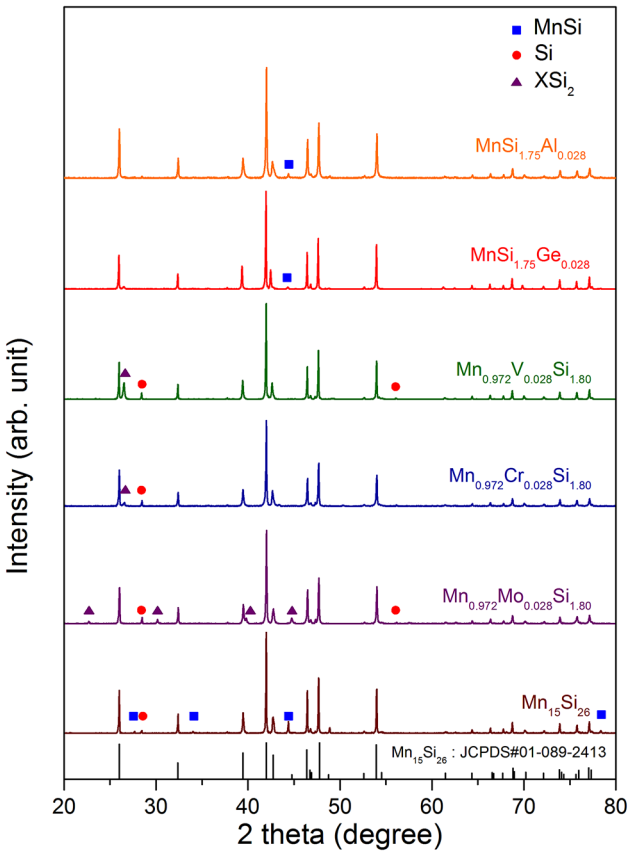

Fig. 1. Powder XRD patterns of SPSed HMS samples doped by Al, Ge, V, Cr and Mo and undoped $Mn_{15}Si_{26}$.

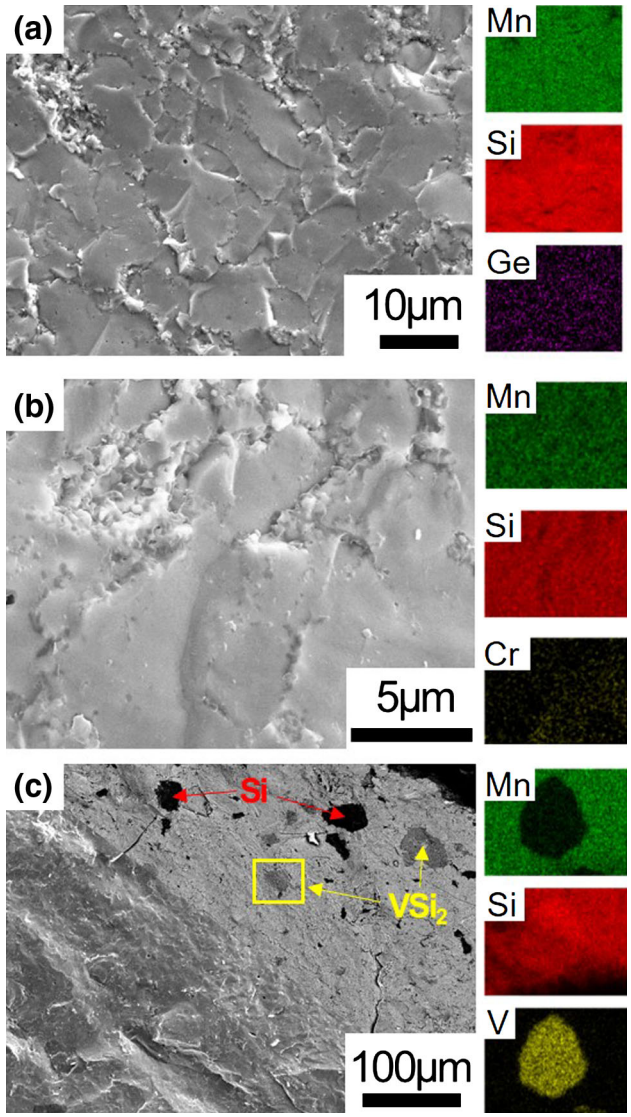

Fig. 2. SEM images of the fractured surface and elemental maps of (a) $MnSi_{1.75}Ge_{0.028}$ (b) $Mn_{0.972}Cr_{0.028}Si_{1.80}$ and (c) SEM image of the fractured surface (lower-left), back scattered electron image (upper-right) and elemental maps of boxed area of $Mn_{0.972}V_{0.028}Si_{1.80}$.

wt.%), and $Mn_{0.972}Cr_{0.028}Si_{1.80}$ (2.76 wt.%), which was calculated using Rietveld refinement. This suggests that V and Mo exist as VSi_2 and $MoSi_2$ rather than substituted at the Mn-site, whereas Al, Ge and Cr might be formed as solid solution with HMS. These results were also found in SEM/EDS data. We could not find any evidence for the formation of secondary phases in $MnSi_{1.75}Ge_{0.028}$ (Fig. 2a) and $Mn_{0.972}Cr_{0.028}Si_{1.80}$ (Fig. 2b), suggesting that Ge and Cr are predominantly substituted at Si- and Mn-sites. In comparison, Si and VSi_2 precipitates (5–50 μm) are clearly observed in back scattering electron images (BSEI) and EDS analysis of $Mn_{0.972}V_{0.028}Si_{1.80}$ (Fig. 2c), indicating that V is highly insoluble in the HMS matrix. On the other hand, the average grain size of SPSed bulks was about 10 μm with highly dense microstructure due to relatively high sintering temperature.

Figure 3a shows the temperature dependence of σ for the pristine $Mn_{15}Si_{26}$ and Al-, Ge- and Cr-doped $Mn_{15}Si_{26}$. All doped samples exhibited the higher σ than that of the pristine sample within the whole measured temperature range. To clarify this, we measured p_H and μ_H of Al-, Ge- and Cr-doped $Mn_{15}Si_{26}$ at 300 K, and represented them in Table I. All doped $Mn_{15}Si_{26}$ samples exhibit higher p_H (1.9–2.9 $\times$ 10^{21} cm^{-3}) values than that of $Mn_{15}Si_{26}$ ($\sim$1.68 $\times$ 10^{21} cm^{-3}). The increased p_H by Al- or Cr-doping indicates that Al^{3+} at Si^{4+}-site or Cr^{6+} at Mn^{7+}-site act as hole donors. On the other hand, although Ge is an isoelectric element, the value of p_H in Ge-doped $Mn_{15}Si_{26}$ was largely increased compared to Al- or Cr-doped compounds due to the difference of the covalent radius between Ge and Si (r_{Ge} = 1.22 Å, r_{Si} = 1.10 Å) occurring for the lattice distortion and variation of bonding.[5] Thus, the higher σ in Ge-doped $Mn_{15}Si_{26}$ would be originated from increased p_H despite relatively lower μ_H. Furthermore, due to the optimized sintering conditions, highly dense microstructures would affect σ positively and exhibit higher values of σ than the best performing doped HMS samples reported previously.

Figure 3b shows the temperature dependence of S (inset) and power factor for $Mn_{15}Si_{26}$ and Al-, Ge-

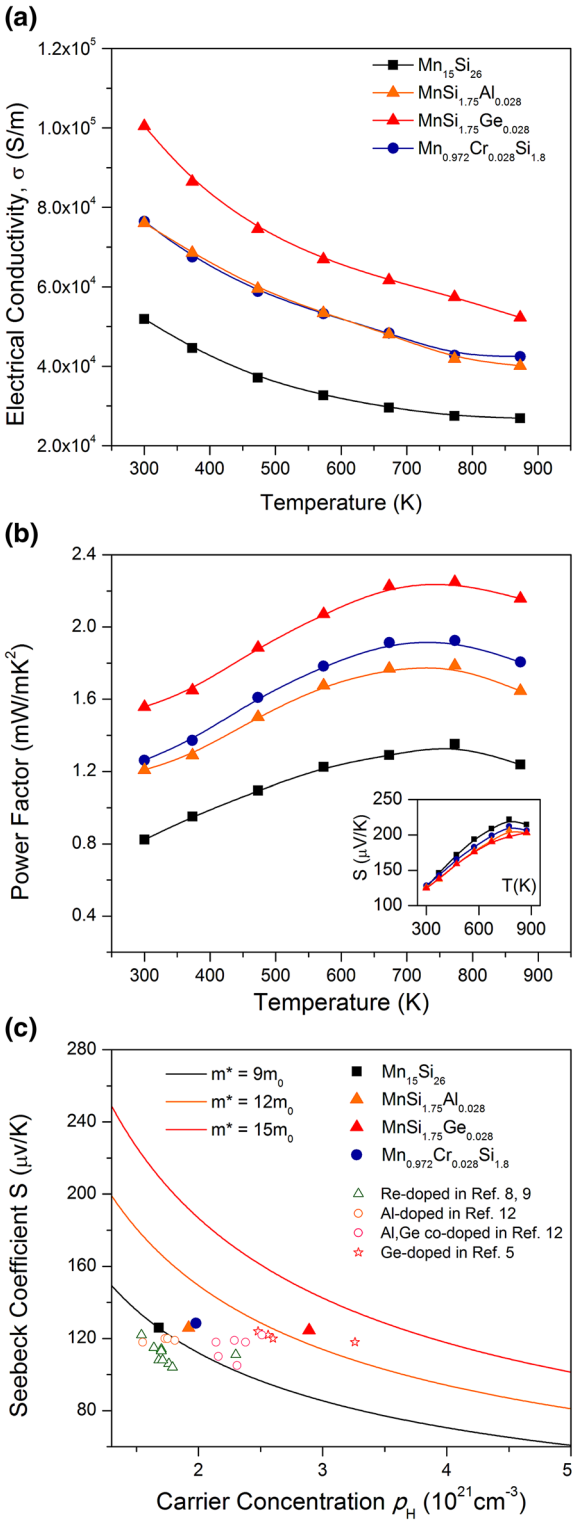

Fig. 3. Temperature dependences of (a) electrical conductivity and (b) power factor for $Mn_{15}Si_{26}$, Al-, Ge- and Cr-doped $Mn_{15}Si_{26}$. The inset in (b) shows the temperature dependence of the Seebeck Coefficient. (c) Seebeck coefficient as a function of carrier concentration (Pisarenko plot) at 300 K for $Mn_{15}Si_{26}$, Al-, Ge- and Cr-doped $Mn_{15}Si_{26}$.

and Cr-doped $Mn_{15}Si_{26}$. As shown in the inset of Fig. 3b, all compounds including undoped HMS exhibit positive S values, which indicates a p-type semiconductor. Although the absolute values of S of doped $Mn_{15}Si_{26}$ decreased mainly due to the increase in p_H, it had less impact on the whole electronic transport properties, which is clearly seen in the plot of the power factor. Compared with $Mn_{15}Si_{26}$ ($\sim$1.35 mW m^{-1} K^{-2} at 773 K), significantly enhanced power factor values from $\sim$ 1.78 mW m^{-1} K^{-2} to $\sim$2.25 mW m^{-1} K^{-2} at 773 K were obtained in doped $Mn_{15}Si_{26}$, indicating the modification of density of states (DOS) by doping. To elucidate this, the DOS effective mass value m^* was estimated from the measured S and p_H using the following Eq. 1 with assuming a SPB model.[17]

$$S = \frac{8\pi^2 k_B^2}{3eh^2}\left(\frac{\pi}{3p_H}\right)^{2/3} m^* T, \quad (1)$$

Here, k_B, e, and h are the Boltzmann constant, elementary charge, and the Planck constant, respectively. Figure 3c and Table I represent the relationship between the measured S and p_H for all compounds at 300 K with some previously reported data on doped HMS. The calculated m^* of the $Mn_{15}Si_{26}$ is 9.01m_0, whereas m^* values of doped $Mn_{15}Si_{26}$ were increased in values of 9.85m_0 (Al-doped $Mn_{15}Si_{26}$), 10.26m_0 (Cr-doped $Mn_{15}Si_{26}$), and 12.79m_0 (Ge-doped $Mn_{15}Si_{26}$). It is considered to be related with the larger m^* for doped $Mn_{15}Si_{26}$ are due to the modification of band structure or Fermi level.

Figure 4a and b show the temperature dependence of κ and κ_{lat} for $Mn_{15}Si_{26}$ and Al-, Ge- and Cr-doped $Mn_{15}Si_{26}$. The magnitude of κ for doped $Mn_{15}Si_{26}$ for the whole measured temperature range was similar, and higher than that of $Mn_{15}Si_{26}$ due to the increased κ_{ele}. To evaluate the point defect phonon scattering effect by doping elements, we calculated the κ_{lat} values by subtraction of κ_{ele} from κ. The κ_{ele} values were estimated using the Wiedemann–Franz law ($\kappa_{ele} = L\sigma T$). The Lorenz number (L) is obtained from Eq. 2 and is approximately 1.8 $\times$ 10^{-8} V^2 K^{-2},

$$L = \left(\frac{k_B}{e}\right)^2 \left(\frac{(r+7/2)F_{r+5/2}(\eta)}{(r+3/2)F_{r+1/2}(\eta)} - \left[\frac{(r+5/2)F_{r+3/2}(\eta)}{(r+3/2)F_{r+1/2}(\eta)}\right]^2\right), \quad (2)$$

where r is the scattering parameter from the temperature dependence of μ_H, $F_n(\eta)$ is the Fermi integral a function of Fermi level η, respectively. As shown in Fig. 4b, calculated κ_{lat} values of Ge-doped $Mn_{15}Si_{26}$ ($\sim$1.95 W m^{-1} K^{-1} at 373 K, $\sim$1.91 W m^{-1} K^{-1} at 773 K) were slightly lower than those of the pristine $Mn_{15}Si_{26}$ ($\sim$2.05 W m^{-1} K^{-1} at 373 K, $\sim$2.08 W

Table I. Hall coefficient R_H, Hall carrier concentration p_H, Hall mobility μ_H and effective mass m^* at 300 K for $Mn_{15}Si_{26}$, Al-, Ge- and Cr-doped $Mn_{15}Si_{26}$

Samples	R_H (10^{-9} m^3 C^{-1})	p_H (10^{21} cm^{-3})	μ_H (cm^2/V^{-1} s^{-1})	m^*/m_0
$Mn_{15}Si_{26}$	3.66	1.68	2.60	9.014
Al-doped	3.21	1.92	2.44	9.849
Ge-doped	2.13	2.89	2.14	12.790
Cr-doped	3.10	1.98	2.37	10.262

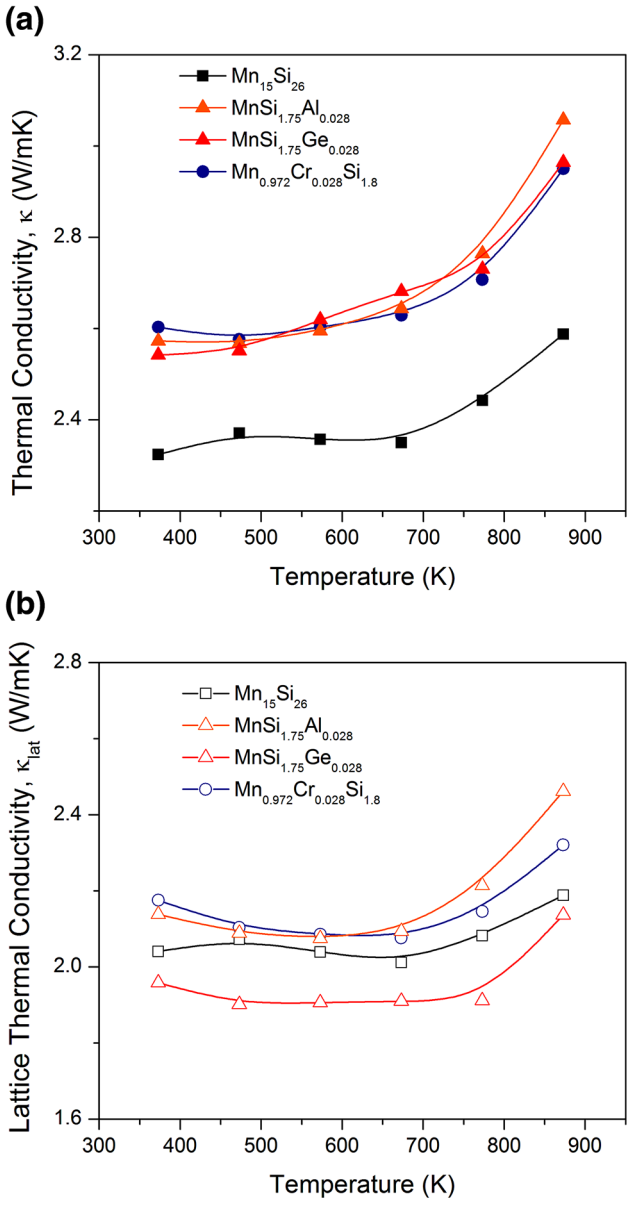

Fig. 4. Temperature dependences of (a) the total thermal conductivity κ and (b) the lattice thermal conductivity κ_{lat} for $Mn_{15}Si_{26}$, Al-, Ge- and Cr-doped $Mn_{15}Si_{26}$.

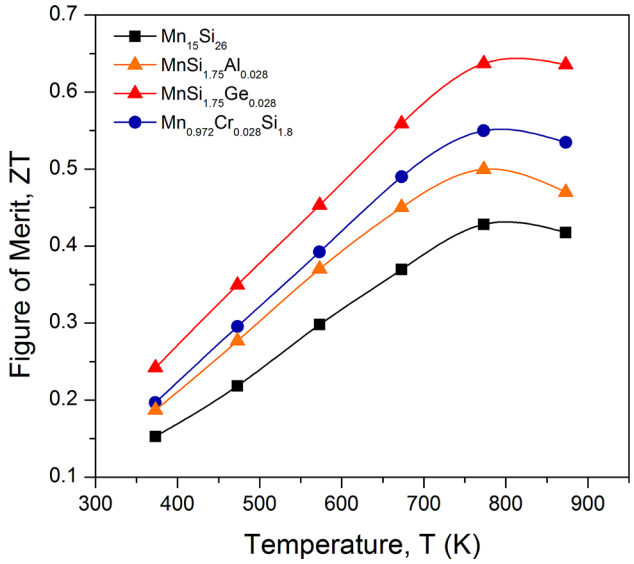

Fig. 5. Temperature dependence of the figure of merit ZT for $Mn_{15}Si_{26}$, Al-, Ge- and Cr-doped $Mn_{15}Si_{26}$.

m^{-1} K^{-1} at 773 K) within the whole measured temperature range. This is considered to be related to the intensified phonon scattering by mass difference between Si (M_{Si} = 28.08) and Ge (M_{Ge} = 72.63). From the measured σ, S, and κ, we calculated ZT values for undoped and doped $Mn_{15}Si_{26}$ samples, and they are presented in Fig. 5. Significantly enhanced ZT values over a wide temperature range were observed in the Ge-doped $Mn_{15}Si_{26}$ ($MnSi_{1.75}Ge_{0.028}$) which reached the peak ZT value of 0.64 at 773 K. This value is comparable to the Ge-doped HMS sample synthesized by induction melting combined with hot-press sintering[4] and thermal explosion followed by the plasma activated sintering technique.[5] In addition to these results, the synthetic conditions, ZT values, and electronic transport parameters (σ, S, p_H, μ_H, m^*) of the present samples and the previously reported materials[4,5,7,11,12,18] are summarized in Table II. Overall, Ge-doped HMS samples exhibit more enhanced thermoelectric properties than other substituted HMS samples mainly due to larger m^*. Interestingly, we obtained higher σ value than

Table II. Synthetic conditions, compositions, electrical transport properties (σ, S, p_H, μ_H, m^*) at 300 K and peak ZT of the HMS-based materials prepared by different research groups

References	Synthetic condition	Composition	σ (S/cm)	S (μV/K)	p_H (10^{21} cm^{-3})	μ_H (cm^2/V s^{-1})	m^*/m_0	ZT
This work	Solid state reaction (SSR) and spark plasma sintering (SPS)	$MnSi_{1.75}Ge_{0.028}$	1005	125	2.89	2.14	12.79	0.64 (773 K)
		$Mn_{0.972}Cr_{0.028}Si_{1.80}$	765	128	1.98	2.37	10.26	0.55 (773 K)
		$MnSi_{1.75}Al_{0.028}$	761	126	1.92	2.44	9.85	0.50 (773 K)
Zhou et al.[4]	Induction melting and hot pressing (HP)	$MnSi_{1.72}Ge_{0.014}$	642	120	1.64	2.44	8.45	0.60 (833 K)
She et al.[5]	Thermal explosion and plasma activated sintering (PAS)	$MnSi_{1.72}Ge_{0.026}$	764	122	2.56	1.86	12.14	0.62 (840 K)
Ponnambalam et al.[7]	Arc melting and HP	$Mn_{0.97}Cr_{0.03}Si_{1.74}$	714	118	2.20	2.00	10.10	0.60 (850 K)
Luo et al.[11]	Melt spinning (MS) and SPS	$MnSi_{1.80}Al_{0.003}$	628	132	1.16	2.44	7.38	0.65 (800 K)
Chen et al.[12]	SSR and SPS	$MnSi_{1.79}Al_{0.005}$	545	118	1.81	1.88	8.87	0.57 (833 K)
		$MnSi_{1.76}Al_{0.004}Ge_{0.032}$	586	115	2.38	1.54	10.38	0.57 (833 K)
Nhi Trung et al.[18]	Mechanical alloying (MA) and SPS	$MnSi_{1.75}Ge_{0.02}$	588	133	–	–	–	0.32 (815 K)
		$Mn_{0.98}Mo_{0.02}$ $Si_{1.75}Ge_{0.02}$	637	130	–	–	–	0.40 (815 K)
		$Mn_{0.98}W_{0.02}$ $Si_{1.75}Ge_{0.02}$	641	118	–	–	–	0.35 (815 K)
		$MnSi_{1.73}Al_{0.02}Ge_{0.02}$	606	128	–	–	–	0.38 (815 K)

those of other doped HMSs, suggesting that electronic transport properties could be tuned by the optimization of processing conditions.

CONCLUSIONS

We investigated the phase formation, microstructure and thermoelectric properties of HMS $Mn_{15}Si_{26}$ doped by Al, Ge, and Cr. It was found that Al, Ge and Cr were homogenously substituted at Mn- and Si-sites without significant generation of secondary phases. An enhanced power factor and a reduced lattice thermal conductivity were simultaneously obtained by Ge-doping due to the increased density of a state's effective mass with optimized carrier concentration and intensified point defect phonon scattering from large mass differences between host Si and doped Ge atoms. A peak ZT value of 0.64 was obtained at 773 K for $MnSi_{1.75}Ge_{0.028}$. We demonstrated that for a simple and scalable fabrication method, the conventional solid state reaction followed by the spark plasma sintering technique, is viable for HMS-based thermoelectric materials. Furthermore, several compositions were found as stable compositions and, thus, could be suggested as effective matrix compositions for nanostructured HMS.

ACKNOWLEDGEMENTS

This work was supported by the Korea government (MSIP) (2014R1A2A1A10053869), the Priority Research Centers Program (2009-0093823) through the National Research Foundation of Korea (NRF), and the Industrial Fundamental Technology Development Program (10052977) funded by the Ministry of Trade, Industry and Energy (MOTIE) of Korea.

REFERENCES

1. I. Nishida, *J. Mater. Sci.* 7, 435 (1972).
2. M.I. Fedorov and V.K. Zaitsev, *Thermoelectrics Handbook: Macro to Nano*, ed. D.M. Rowe (Boca Raton: CRC Press, 2006), p. 31.
3. X. Chen, A. Weathers, J. Carrete, S. Mukhopadhyay, O. Delaire, D.A. Stewart, N. Mingo, S.N. Girard, J. Ma, D.L. Abernathy, J. Yan, R. Sheshka, D.P. Sellan, F. Meng, S. Jin, J. Zhou, and L. Shi, *Nat. Commun.* 6, 6723 (2015).
4. A.J. Zhou, T.J. Zhu, X.B. Zhao, S.H. Yang, T. Dasgupta, C. Stiewe, R. Hassdorf, and E. Mueller, *J. Electron. Mater.* 39, 2002 (2010).
5. X. She, X. Su, H. Du, T. Liang, G. Zheng, Y. Yan, R. Akram, C. Uher, and X. Tang, *J. Mater. Chem. C* 3, 12116 (2015).
6. G. Bernard-Granger, M. Souler, H. Ihou-Mouko, C. Navone, M. Boidot, J. Leforestier, and J. Simon, *J. Alloys Compd.* 618, 403 (2015).
7. V. Ponnambalam, D.T. Morelli, S. Bhattacharya, and T.M. Tritt, *J. Alloys Compd.* 580, 598 (2013).
8. X. Chen, S.N. Girard, F. Meng, E. Lara-Curzio, S. Jin, J.B. Goodenough, J. Zhou, and L. Shi, *Adv. Energy Mater.* 4, 1400452 (2014).
9. X. Chen, J. Zhou, J.B. Goodenough, and L. Shi, *J. Mater. Chem. C* 3, 10500 (2015).
10. I. Aoyama, M.I. Fedorov, V.K. Zaitsev, F.Y. Solomkin, I.S. Eremin, A.Y. Samunin, M. Mukoujima, S. Sano, and T. Tsuji, *Jpn. J. Appl. Phys.* 44, 8562 (2005).

11. W. Luo, H. Li, W. Hao, and X. Tang, *J. Electron. Mater.* 40, 1233 (2011).
12. X. Chen, A. Weathers, D. Salta, L. Zhang, J. Zhou, J.B. Goodenough, and L. Shi, *J. Appl. Phys.* 114, 173705 (2013).
13. W. Luo, H. Li, Y. Yan, Z. Lin, X. Tang, Q. Zhang, and C. Uher, *Intermetallics* 19, 404 (2011).
14. T. Itoh and M. Yamada, *J. Electron. Mater.* 38, 925 (2009).
15. P. Norouzzadeh, Z. Zamanipour, J.S. Krasinski, and D. Vashaee, *J. Appl. Phys.* 112, 124308 (2012).
16. A. Pokhrel, Z.P. Degregorio, J.M. Higgins, S.N. Girard, and S. Jin, *Chem. Mater.* 25, 632 (2013).
17. G.J. Snyder and E.S. Toberer, *Nat. Mater.* 7, 105 (2008).
18. D.Y. Nhi Trung, D. Berthebaud, F. Gascoin, and H. Kleinke, *J. Electron. Mater.* 44, 3603 (2015).